Theoretical study of the quenching of NH (¹Δ) molecules via collisions with Rb atoms

Daniel J. Haxton,[*] Steven A. Wrathmall,[†] H. J. Lewandowski,[‡] and Chris H. Greene[§]

Department of Physics and JILA, University of Colorado, Boulder, Colorado 80309, USA

(Received 23 March 2009; published 14 August 2009)

We examine the quenching reaction $Rb(^2S) + NH(^1\Delta) \to Rb(^2P_{1/2}) + NH(X\,^3\Sigma^-)$. This reaction may be utilized to produce ground-state NH molecules for studies of ultracold physics or for other purposes and is interesting in that it involves initial and final states that are nearly degenerate. This near degeneracy is expected to lead to a large reaction rate. We examine this system using *ab initio* quantum chemistry calculations and scattering calculations, which include spin-orbit effects, and find that the reaction rate is large and, in fact, approaches the quantum-mechanical unitarity limit. We discuss the prospects for an experimental examination of this system.

I. INTRODUCTION

Chemical reactions involving free-radical molecules are important in many dense gas systems including combustion gases [1] and interstellar clouds [2,3]. The fundamental imidogen free radical (NH) has been detected [4] as an intermediate in the combustion of CH_4 with N_2O. NH has a ground-state triplet, $X\,^3\Sigma^-$, and a long-lived metastable state [5], the singlet delta, labeled $a\Delta^1$ or $^1\Delta$. This state is doubly forbidden to decay via electric dipole radiation ($^1\Delta \to X\,^3\Sigma^-$), making it amenable to laboratory study [6].

In addition, there is currently considerable interest in collisions between diatomic molecules, such as NH, and alkalimetal atoms. This interest stems from the relevance of such systems to ultracold physics and chemistry [7–13] and the increased level of control possible through the use of cooling and trapping techniques. The advent [14] of the Bose-Einstein condensate (BEC) led to the production of mixed BECs [15] and engendered work on production and trapping of cold molecules [16–19]. There has been considerable recent experimental work on creating cold dipolar molecular samples for collision studies. For example, cold OH [20] and NH molecules in either the ground ($^3\Sigma^-$) or the $^1\Delta$ electronic state [21–25] have been produced. In addition, there are a growing number of theoretical investigations on interactions between diatomic molecules and alkali-metal atoms. A broad survey of interactions of alkali and alkaline-earth metals with NH was published in Ref. [26]. Other theoretical works on the Rb-NH system involved examinations of the relevant potential-energy surfaces [27–29]. Explorations have also been conducted for related systems such as Rb-OH [30,31], He-NH [32–34], Rb-NH_3 [35,36], and NH-NH [37].

Our interest aims toward a broad treatment of the Rb-NH system, including up to the first excited electronic states of both the atom and the molecule. We have constructed a preliminary treatment and present some initial results here. The goal is to accurately calculate the dynamics on the higher

excited electronic states. In particular, we concentrate on the states $^3\Sigma^-$ and $^1\Delta$ of NH and the states ^2S, $^2P_{1/2}$, and $^2P_{3/2}$ of Rb. As it happens, the excitation energies from the ^2S state to the ^2P state are nearly equal to the excitation energy of NH, such that the channels are unusually close in energy; in fact, the excited NH channel lies between the two spin-orbit components of the Rb ^2P state. Specifically, the excitation energies are 12 687.8 cm^{-1} on NH [5] and 12 578.96 and 12 816.55 cm^{-1} for Rb $^2P_{1/2}$ and $^2P_{3/2}$, respectively [38].

This situation makes the quenching of the excited NH ($^1\Delta$) state by Rb, using the reaction

$$Rb\ (^2S) + NH\ (^1\Delta) \to Rb\ (^2P) + NH\ (X\,^3\Sigma^-), \quad (1)$$
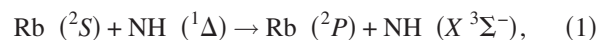
an interesting one to study for several reasons. First, it opens up the possibility that this quenching reaction could find some use in ultracold physics, as it would represent an electronically inelastic reaction at cold initial and final collision energies. This is a chemically reactive process, in the sense that the chemical nature of the products is dramatically different from that of the reactants. Second, it could prove useful as a mechanism for producing ground-state NH from the exited state.

This quenching reaction can be precisely studied using techniques to cool and to trap atomic and molecular samples. The methods of atom cooling and trapping have been refined over the last 15 years such that one can routinely produce dense samples (up to 10^{13} cm^{-3}) with temperatures on the order of 1–100 μK. More recently, with the development of Stark deceleration of polar molecules [39], trapped molecular samples can be produced with temperatures on the order of 1–100 mK.

An experimental realization will proceed as follows. The atoms will be cooled in a magneto-optical trap and transferred to quadrupole magnetic trap in one region of the vacuum system. During this process, a pulsed beam of NH molecules will be slowed using a Stark decelerator and trapped using electrostatic fields [40]. Because of the weak interaction between the atom and the electric field, the two species can be controlled independently. This control will allow the atoms to be moved to overlap the molecular sample, setting the initial time for the interaction. There will be several methods of detection employed in order to gain a

---

*dhaxton@jila.colorado.edu
†steven.wrathmall@jila.colodado.edu
‡lewandoh@jilau1.colorado.edu
§chris.greene@colorado.edu

TABLE I. Electronic microstates considered in our study: quantum numbers at linear geometry. Each is a member of a different Kramers doublet. The quantum numbers also label the members of our diabatic basis for all geometries and the electronic channels of the scattering calculation. The quantum numbers $|\Omega|$ and Σ are the absolute values of the projection of the total and the spin angular momenta on the NH axis.

			Doublets			
(1)	$^1\Delta(^1\Delta \times {}^2S)|\Omega|=\frac{3}{2}$	(2)	$^2\Delta(^1\Delta \times {}^2S)|\Omega|=\frac{5}{2}$	(3)	$^2\Sigma(^3\Sigma^- \times {}^2S)$	
(4)	$^2\Pi$ anion $|\Omega|=\frac{1}{2}$	(5)	$^2\Pi$ anion $|\Omega|=\frac{3}{2}$			
			NH $^3\Sigma^- \times$ Rb ^2P, $|\Omega|=\frac{1}{2}$			
(6)	$\Sigma^{\mathrm{NH}}=0$ Rb $^2P_{3/2}^{(1/2)}$	(7)	$\Sigma^{\mathrm{NH}}=1$ Rb $^2P_{3/2}^{(1/2)}$	(8)	$\Sigma^{\mathrm{NH}}=0$ Rb $^2P_{1/2}^{(1/2)}$	
(9)	$\Sigma^{\mathrm{NH}}=1$ Rb $^2P_{3/2}^{(3/2)}$	(10)	$\Sigma^{\mathrm{NH}}=1$ Rb $^2P_{1/2}^{(1/2)}$			
			NH $^3\Sigma^- \times$ Rb ^2P, $|\Omega|=\frac{3}{2}$			
(11)	$\Sigma^{\mathrm{NH}}=0$ Rb $^2P_{3/2}^{(3/2)}$	(12)	$\Sigma^{\mathrm{NH}}=1$ Rb $^2P_{1/2}^{(1/2)}$	(13)	$\Sigma^{\mathrm{NH}}=1$ Rb $^2P_{3/2}^{(1/2)}$	
			NH $^3\Sigma^- \times$ Rb ^{2}P, $|\Omega|=\frac{5}{2}$			
(14)	$\Sigma^{\mathrm{NH}}=1$ Rb $^2P_{3/2}^{(3/2)}$					
			$^4\Sigma$ (NH $^3\Sigma^- \times$ Rb ^{2}S)			
(15)	$\Sigma=|\Omega|=\frac{1}{2}$	(16)	$\Sigma=|\Omega|=\frac{3}{2}$			

full understanding of the interaction. A novel signature of this reaction is the photon produced from the decay of the excited atom $(^2P_{1/2} \rightarrow {}^2S_{1/2})$. This dipole-allowed transition will happen very rapidly after the collisional excitation of Rb. These photons can be detected efficiently with almost no background using a spectrally filtered photomultiplier tube. In addition, both the number and the temperature of the trapped atom sample can be measured with absorption imaging, while the number and the temperature of the molecular sample can be measured with resonance enhanced multiphoton ionization (REMPI). Through this procedure, it should be possible to measure the reaction rate.

II. QUANTUM CHEMISTRY CALCULATIONS

We carry out quantum chemistry calculations using the COLUMBUS package [41–43] for calculations on the electronic states of the Rb-NH system. We use an effective core potential [44,45] that accounts for the 36 core electrons of Rb, and thus treats the Rb atom as a one-electron system. We therefore perform calculations on nine-electron states. We adjust our effective core potential to reproduce the correct channel energies of the combined Rb-NH system at infinite separation.

For the moment we have constructed a set of two-dimensional potential-energy surfaces, fixing the NH bond length at $1.925a_0$. We refer to the configuration of the Rb-NH molecule using Jacobi coordinates. These coordinates are defined as r, the NH bond distance, $1.925a_0$; R, the distance between the NH center of mass and Rb; and γ, the angle between the two corresponding vectors, such that $\gamma =0$ denotes a linear Rb-H-N configuration.

Owing to our use of a pseudopotential, in addition to the large number of electronic states treated by a relatively modest configuration-interaction (CI) calculation, the surfaces we construct are not expected to be of "spectroscopic accuracy"

but instead probably have errors on the order of tens of meV. They are expected to be sufficiently accurate for the qualitative study presented here and, in any case, the omission of motion in the Jacobi r_{NH} degree of freedom surely compromises the calculated dynamics more than does any error in the potential-energy surfaces.

All in all, and without considering spin-orbit coupling, there are eight doublet states and four quartet states, for a total of 32 microstates. This odd electron system enjoys the Kramers degeneracy and thus the electronic Hilbert space is block diagonal in two 16×16 blocks. For the total angular momentum $J=0$, we need only to consider one of these blocks. The asymptotes of the adiabatic states are listed in Table I.

At linear geometry, the electronic states are described by their projections of angular momentum on the molecular axis. We refer to the electronic states by the standard Λ, Ω, and Σ quantum numbers. Λ is the absolute value of the projection of electronic angular momentum on the molecular axis—the eigenvalue of the operator $\hat{l}_z$, such that $\Lambda=2$ denotes a Δ state, etc. $|\Omega|$ is the absolute value of the projection of the total angular momentum on the molecular axis—the eigenvalue of the operator $\hat{j}_z = \hat{l}_z + \hat{s}_z$. The absolute value of the eigenvalue of $\hat{s}_z$ is denoted by Σ. The symbol Σ is also used to denote a state with $\Lambda=0$, but we will avoid ambiguity by always denoting the multiplicity of a given electronic state as in $^2\Sigma$.

The Born-Oppenheimer electronic states are first calculated without spin-orbit coupling. The next step is a diabatization [46] of these potentials, in which we construct diabatic states labeled primarily by integer values of Λ, by diagonalizing the electronic angular momentum $\hat{l}_z$ projected onto the NH axis. $\pm\Lambda$ is thus not only the eigenvalue of the projection of angular momentum at linear geometry for a given diabatic electronic state, but also its approximate expectation value at other geometries. We have a pair of $^2\Delta$

diabatic states, two pairs of $^2\Pi$ states, and two $^2\Sigma$ states. The doublet Π states are distinguished as anionic in character (NH$^- \times$Rb$^+$) or not (NH $^3\Sigma^- \times$ Rb ^2P). The Σ states are essentially NH $^3\Sigma^-$ times Rb in either the ground ^2S state or the $^2P_\sigma$ state. We also have two $^4\Sigma$ and one $^4\Pi$ state.

A diabatization is useful to us for two reasons. First, it allows for the convenient inclusion of nonadiabatic effects among the adiabatic surfaces, accounting for conical intersections, for instance. Rovibronic effects such as the Renner-Teller effect can also be accounted for by such a diabatization, although at this stage we do not include the mixing of electronic and rotational angular momenta.

Second, it appears to allow us to add the spin-orbit terms "by hand," and therefore enables us to perform a larger electronic structure calculation, although we employ a smaller calculation using the spin-orbit CI capability of COLUMBUS to verify the accuracy of this procedure. The final steps in constructing the surfaces are then the addition of spin-orbit terms to the diabatic electronic Hamiltonian and, lastly, the transformation to a representation that accounts for the Kramers degeneracy.

A. Details

We have found it prohibitive to use a basis set large enough to get a sufficiently accurate NH excitation energy. Therefore, in order to reproduce the physical energetics, we artificially modify the effective Rb core potential. We begin with the Dirac-Fock pseudopotential developed in Refs. [44,45]. The pseudopotential for the S and the P waves is then modified by changing their functional forms into

$$s: 45.272 \exp(-1.012 r^2) \rightarrow 45.272 \exp(-1.149\,730\,57 r^2),$$

$$p: 2.83 \exp(-0.3036 r^2) \rightarrow 2.83 \exp(-0.267\,230\,608 r^2)$$
$$(2)$$

An uncontracted Dirac-Fock basis set is adopted for the Rb; while for N and H we use the augmented correlation consistent polarized valence triple zeta basis set of Dunning [47]. The excitation energies obtained are approximately 12 98(5) cm^{-1} on both the Rb (without spin-orbit interaction) and the NH fragments.

The electronic configuration of the NH states of interest is $1s^2 2s^2 2p_\sigma^2 2p_\pi^2$. In addition to these orbitals, we have the four orbitals on rubidium (s and p), for a total of nine orbitals in the valence space. To describe all of these states for all geometries, it is necessary to include orbitals beyond the minimum set of nine $1-5\sigma$ and $1-2\pi$ orbitals. The anion state is the highest in energy at infinite Rb-NH separation, but becomes the ground state at small Rb-NH separation, and it undergoes avoided crossings with all of the other states and so is relevant to the dynamics on the other surfaces. To describe the anion state, two additional orbitals are necessary: a π relaxation orbital that accounts for the expansion of the NH π orbitals in the anion state relative to the neutral states and a correlating σ^* orbital on the NH which increases the Rb-NH bonding on the anion surface. In Ref. [27] a similar

orbital space was used although what we denote as an anion relaxation orbital was denoted by those authors as a $6p$ orbital.

For the first step, a state-averaged multiconfiguration self consistant field calculation in the minimum nine-orbital space is performed on the lowest six doublet states and the four quartets. This calculation produces a π orbital on the NH fragment that does not account for the relaxation within the anion state; that calculation significantly overestimates the anion state energy at small Rb-NH separations.

The next step is an all-singles-and-doubles CI calculation on the eight doublets and four quartets in which we are interested. At large R, we must follow the anion state surface as it rises above several states that we are not interested in. Twelve averaged natural orbitals are adopted from this CI calculation, expanding the orbital space to include both the π relaxation orbitals and the σ^* correlating orbital. We then perform an all-singles-and-doubles CI calculation in this space of twelve natural orbitals. In both CI steps we freeze the $1-2a'$, also known as the $1-2\sigma$, orbitals on NH, which are basically N $1s$ and $2s$. Among the four sets of spin and space symmetries, the maximum number of configuration state functions in the CI is 1 110 312 for the doublet A'.

B. Diabatization

At this stage of the calculation there are twelve adiabatic electronic states as functions of nuclear geometry (eight doublets and four quartets), and the spin-orbit terms have not yet been added. A unitary transformation is now applied to these twelve states, a property-based diabatization [46,48,49].

The doublets are diabatized using both the electronic dipole operator and the z projection of the orbital angular momentum relative to the NH bond axis (the $\widehat{l_z}$ operator with eigenvalue $\pm\Lambda$ at linear geometry). The $\widehat{l_z}$ operator is first diagonalized in the adiabatic basis. In order to prevent an avoided crossing at large Rb-NH separations that would lead to a problematic mixing of our diabatic basis, a column and a row of the $\widehat{l_z}$ matrix must be damped. This transformation of the $\widehat{l_z}$ operator does not affect the eigenvectors, except near the avoided crossings. The matrix elements of $\widehat{l_z}$ in the ground-state A'' row and column are thus reduced by hand beyond $R = 10.4 a_0$. At such large internuclear separations, the lowest A'' state is Rb(^2S)+NH($^3\Sigma^-$). We reduce the matrix elements in this row and column by a geometry-dependent factor

$$\forall_i \quad \begin{matrix} \widehat{(l_z)}_{i,1} \rightarrow \widehat{(l_z)}_{i,1} \\ \widehat{(l_z)}_{1,i} \rightarrow \widehat{(l_z)}_{1,i} \end{matrix} \times \begin{cases} 1, & R\sin\theta \le 10.4 a_0 \\ \dfrac{10.4}{R\sin\theta}, & R\sin\theta \ge 10.4 a_0. \end{cases}$$
$$(3)$$

With this damping function, the mixing between the two states NH ($^3\Sigma^-$) times Rb (^2S) or ($^2P_{A''}$) is suppressed and
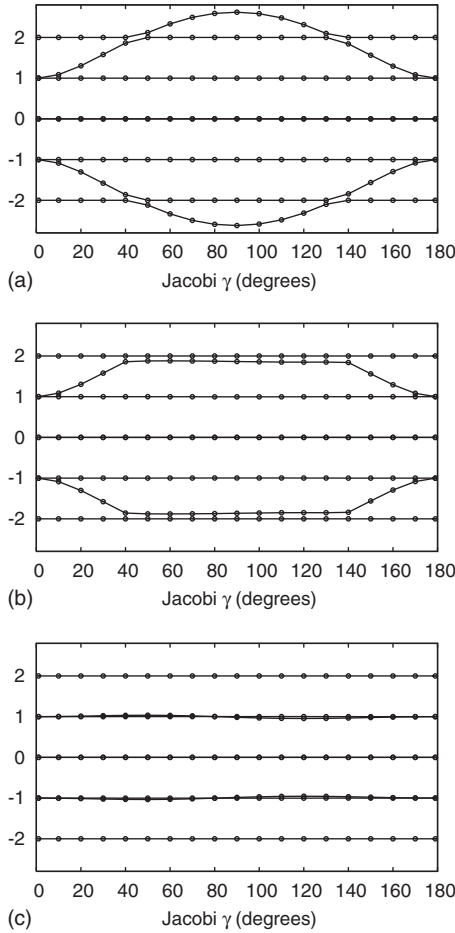
FIG. 1. Eigenvalues and expectation values of the operator $\widehat{l_z}$ for diabatic states evaluated at $R_{\text{Rb-NH}} = 16.0a_0$ as a function of the Jacobi angle γ. (a) Eigenvalues in the adiabatic basis. (b) Eigenvalues in the adiabatic basis with damping function of Eq. (3). (c) Expectation values of $\widehat{l_z}$ for final diabatic states. The absolute values of these numbers provide the Λ labels of the diabatic states ($^2\Sigma, ^2\Pi, ^2\Delta$).

the nonionic Π state has a $\widehat{l_z}$ eigenvalue, which plateaus around 1.85.

Figure 1 shows the eigenvalues of $\widehat{l_z}$ for the doublets only. Figure 1(a) depicts the eigenvalues of $\widehat{l_z}$ in the adiabatic basis at $R = 16.0a_0$. The $\widehat{l_z}$ eigenvalues using the damping function are plotted in Fig. 1(b). The final expectation values of $\widehat{l_z}$ in our diabatic basis are shown in Fig. 1(c); these values are nearly integers, which permits the labeling of these states by the Λ quantum number labels. We have a total of two $^2\Sigma$, two $^2\Pi$, and one $^2\Delta$ and two $^4\Sigma$ and one $^4\Pi$ diabatic state.

The electronic dipole operator is used to separate the two $^2\Pi$ states. These correlate with the anion NH$^-$($^2\Pi$)+Rb$^+$ state and with NH($X\,^3\Sigma^-$)+Rb(^2P) states at infinity; at small Rb-NH separations the former is the lower electronic state and at large separations the latter is the lower. The interaction

between these states is such that they form an avoided crossing of width approximately 1000 cm^{-1} around $R_{\text{Rb-NH}} = 11a_0$. The situation is similar to that of Rb-OH [30,31]. The diagonalization of the electronic dipole operator in the direction of the Jacobi vector $\vec{R}$ is carried out in the Π^+ and the Π^- spaces separately, and the electronic Hamiltonian is diagonalized in the $^2\Sigma$ space. The quartets are diabatized by the diagonalization of $\widehat{l_z}$, followed by the diagonalization of the electronic Hamiltonian in the $^4\Sigma$ space. The expectation values of $\widehat{l_z}$ in our final diabatic basis are all near integers.

C. Adding spin-orbit terms

At this point, then, we have a diabatic basis in which each member is labeled by a given projection of electronic angular momentum about the NH bond axis, and in which the spin-orbit part of the electronic Hamiltonian has not been included. Including the spin degrees of freedom, we arrive at the full 32-microstate basis. Assuming that our diabatic basis function labels are indeed good quantum numbers, the addition of the spin-orbit terms is straightforward, requiring only the enforcement of the Condon-Shortley phase convention among the members of the diabatic basis, and the spin-orbit terms have no dependence on the nuclear geometry. The discussion below verifies that this approximation faithfully reproduces the true eigenvalues.

After adding these spin-orbit terms we shift the delta diabatic potential-energy surfaces slightly (by tens of wave numbers) such that the asymptotes coincide with their physical values. A unitary transformation now yields the two uncoupled 16×16 blocks each containing one member of every Kramers doublet. These blocks are complex conjugates of one another; it is only necessary to choose one of these to use as the Born-Oppenheimer electronic Hamiltonian for the total angular momentum $J = 0$. Extensions to include the electronic angular momentum (the Renner-Teller and the spin Renner-Teller effects) and nonzero J will instead use the real-valued 32×32 representation.

D. Description of the surfaces

Results of the non-spin-orbit CI for linear Rb-N-H geometry are shown in Fig. 2(a). The ground state in the asymptotic region is Rb(^2S)+NH($X\,^3\Sigma^-$) with an asymptote of −55.199 316 2 hartree.

The $^2\Pi$ anion surface comes sweeping down, with a minimum at $5.1192a_0$ of −55.234 652 3 hartree, giving a depth of 0.949 eV. In comparison, Ref. [27] found a well depth of 1.372 eV at $R = 4.911a_0$, for a NH bond length of $1.948a_0$. It crosses the collection of nearly degenerate channels at approximately $12.0a_0$ and crosses the surface that is asymptotically the ground state at $7.3029a_0$ and at an energy of −55.199 771 2 hartree. In comparison, Ref. [27] found the crossing at $7.163a_0$, also for a NH bond length of $1.948a_0$.

The final results including the spin-orbit interaction, obtained by adding the spin-orbit terms by hand to the diabatic Hamiltonian, are plotted in Fig. 2(b), in a closer view. The $^2\Delta$ state is visible as the flattest line, staying near zero wave
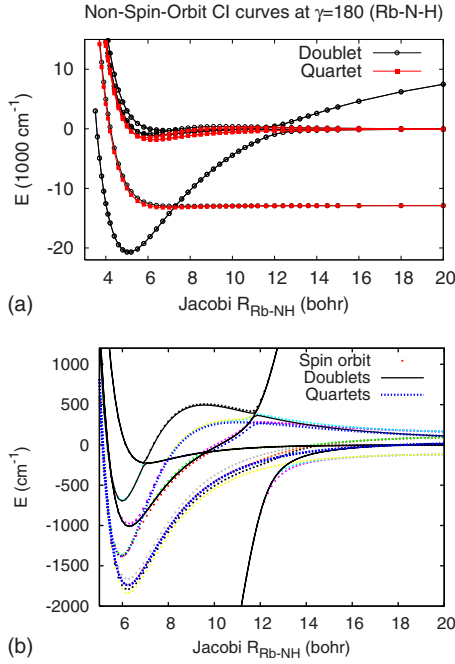
FIG. 2. (Color online) (a) Non-spin-orbit CI results at $\gamma = 180°$. (b) Final spin-orbit surfaces used in the study, obtained by adding the spin-orbit term by hand to the diabatic basis; $\gamma = 180°$.

numbers until around $10a_0$ on the scale of the figure. At the far edge of the figure, the surfaces have separated into the $\mathrm{Rb}(^2S) \times \mathrm{NH}(^1\Delta)$ asymptote, in the middle, with $\mathrm{Rb}\,(^2P_{3/2})$ and $\mathrm{Rb}(^2P_{1/2}) \times \mathrm{NH}(X\,^3\Sigma^-)$ above and below, respectively.

Components of the upper $^2P_{3/2}$ state split into sets following either the $^{2,4}\Sigma$ surface, which rises from its asymptote inward, or the $^{2,4}\Pi$ surfaces. These latter surfaces drop in energy going inward from their asymptote—the quartet less so, whereas the $^2\Pi$ surface undergoes an avoided crossing with the anion $^2\Pi$ surface, dropping steeply downward from the top of the figure. Inward of this avoided crossing around $12.0a_0$, the $^2\Pi\,[(\mathrm{Rb}\,^2P) \times (\mathrm{NH}\,X\,^3\Sigma^-)]$ state is found dropping downward with decreasing R from the avoided crossing and crosses the $^2\Delta$ surface around $9.0a_0$. There are other crossings farther in (too numerous to mention).

The long-range behavior of the surfaces is shown in Fig. 3. This behavior is governed by the long-range interactions: as the NH has a dipole moment, these are dipole- quadrupole with $\frac{1}{r^4}$ power law for the $\mathrm{Rb}\,(^2P)$ fragment and dipole-induced dipole with $\frac{1}{r^6}$ power law for the ^2S fragment. The
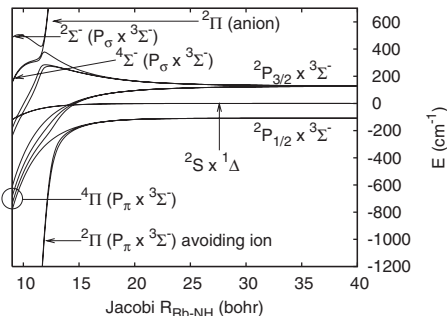
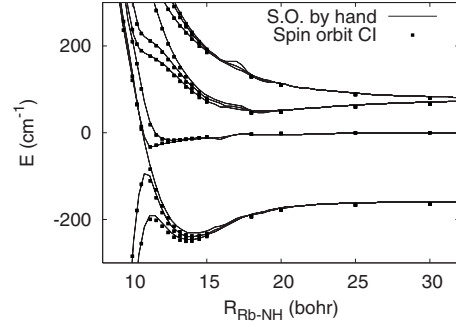

FIG. 3. Long-range behavior of surfaces; $\gamma = 180°$.

FIG. 4. Spin-orbit results using a smaller nine orbital valence space CI; $\gamma = 30°$. Spline-interpolated surfaces calculated from diabatic states adding the spin-orbit interaction by hand (lines) compared with spin-orbit CI results (points). The asymptotes are not correct for this test calculation.

dipole-quadrupole interaction, acting on the $(\mathrm{Rb}\,^2P) \times (\mathrm{NH}\,^3\Sigma^-)$ channels, is stronger than the dipole-induced dipole interaction for the $^2\Delta$ channel and therefore the crossings are determined by the former. At linear Rb-N-H geometry, this interaction splits the ^2P state into the Σ component at higher energy and the Π component at lower energy, which is behavior we described above for the results in Fig. 2(b). It is responsible for the crossings around $14.7a_0$. We examined these crossings for various Jacobi angles γ; for all angles the crossing is apparently too sharp to provide a mechanism for coupling between the $^2\Delta$ and the components of the $\mathrm{Rb}\,(^2P_{3/2})$ state that correlate with Π symmetry farther in. Results below seem to indicate that this is indeed the case. The relevant crossings for collisions at low energy are those visible in Fig. 2(b).

E. Verification of treatment of spin-orbit effect

The spin-orbit calculation using the COLUMBUS program was prohibitively large to perform in the full orbital space. We thus perform the spin-orbit calculation only at the first nine-orbital CI step as described above. Results of this calculation are presented in Fig. 4. These results verify that addition of the spin-orbit terms by hand to the diabatized Hamiltonian from the non-spin-orbit CI calculation reproduces the results of the full spin-orbit CI. (The asymptotes are not correct for the test calculation shown in this figure.)

III. SCATTERING CALCULATION

We calculate the quantum nuclear dynamics on the coupled set of diabatic potential-energy surfaces for the total angular momentum $J = 0$. The standard [50,51] body-fixed Hamiltonian for R times the wave function, keeping r fixed, in Jacobi coordinates is

$$H = -\frac{1}{2\mu_R}\frac{\partial^2}{\partial R^2} + B_r \hat{j}^2 + \frac{1}{2\mu_R R^2}\hat{j}^2 + V(R, r, \gamma),$$

$$\hat{j}^2 = -\left(\frac{1}{\sin(\gamma)}\frac{\partial}{\partial\gamma}\sin(\gamma)\frac{\partial}{\partial\gamma}\right), \tag{4}$$

where μ_R is the reduced mass in that degree of freedom; B_r is the rotational constant of NH, taken to be 16.699 cm^{-1} [52],

which is the value for the ground electronic state; and V is the matrix representation of the electronic Hamiltonian in the diabatic basis.

The scattering calculations employ the R-matrix propagator technique of Baluja *et al.* [53]. Our implementation adopts the discrete variable representation (DVR) [54,55], with the Legendre DVR [56] in γ—with 80 points—and the Gauss-Lobatto DVR [57] in R, with six points per element, 960 elements, from $3.25a_0$ to $43.25a_0$. The propagation covers one element at a time. For each diabatic electronic state, the basis in γ is contracted by the calculation of an adiabatic basis in γ as a function of the scattering coordinate R and include 42 adiabatic states in γ per diabatic electronic state. Slow variable discretization [58] efficiently accounts for the coupling between these surfaces nonadiabatic in R.

Results of the scattering calculation are shown in Fig. 5. The total probabilities for transitions from the ground rovibrational state of NH($^1\Delta$)+Rb(^2S) to the other electronic states are plotted as functions of collision energy in the incident channel. Two degenerate $^2\Delta$ channels in the calculation have $|\Omega| = \frac{3}{2}$ or $\frac{5}{2}$, but the method permits the evaluation of four independent cross sections, for both the calculated and the time-reversed processes corresponding to the other 16×16 Kramers doublet block (i.e., complex conjugating the electronic Hamiltonian in the diabatic basis). The four corresponding sets of scattering amplitudes correspond to two rows and two columns of the calculated S matrix. The S matrix cannot be chosen to be symmetric because we have excluded the time-reversed orthogonal complement of our 16 states, which are the sixteen states of the other Kramers doublet block. The label "TR" in Fig. 5 denotes the time-reversed partner.

These results indicate that the cross section for the quenching reaction is indeed large in the present treatment, and it is in fact comparable to the unitarity limit. In contrast, the cross section to the ground $^{2,4}\Sigma$ channels is significant for low collision energy but is at least an order of magnitude below the quenching reaction cross section at energies above the Rb $^2P_{3/2}$ threshold, which is marked with an arrow on the abscissa of Fig. 5. A qualitative change in the branching ratios becomes evident near this energy, 128 wave numbers; the lower three panels of Fig. 5 indicate that, for collisions in those incident channels, the proportion of Rb(^2P) +NH($^3\Sigma^-$) to Rb(^2S)+NH($^1\Delta$) produced increases at higher energy. However, the correlation of features such as the change in this proportion with the opening of the $^2P_{3/2}$ channels is not perfect, and there is the possibility that it derives from the opening of different channels [for instance, the Rb(^2S)+NH($^1\Delta j$=2) channel at 100 wave numbers or Rb($^2P_{1/2}$)+NH($^3\Sigma^- j$=3) at 91 wave numbers] or another mechanism altogether. A fuller characterization of these results will be presented in a forthcoming publication.

IV. TIME-DEPENDENT CALCULATIONS

Time-dependent calculations help to illustrate the dynamics that drives the quenching reaction. These have been carried out using a smaller basis of 20 adiabatic basis functions in the Jacobi angle γ using 50 Gauss-Legendre DVR basis
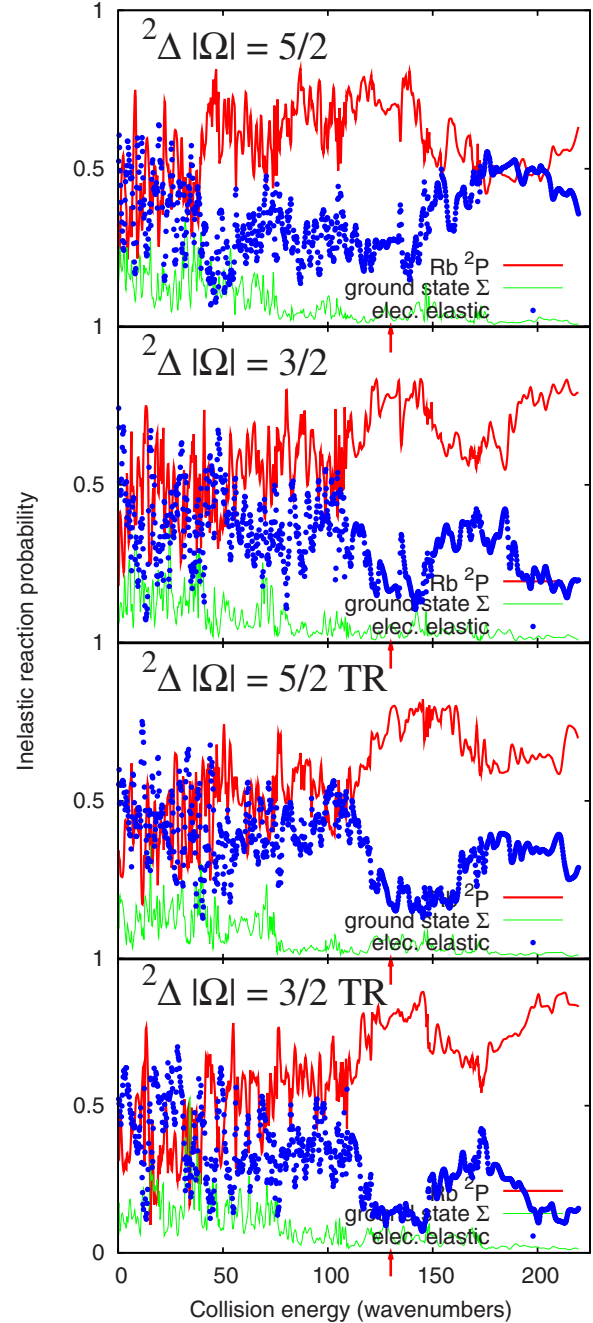

FIG. 5. (Color online) Results of scattering calculations: the probability per collision for a transition from the lowest rovibrational state of $^2\Delta$ (NH $^1\Delta \times$ Rb ^2S) to other electronic states as a function of collision energy, for J=0. The four unique initial states are described in the text. The thick red (dark gray) line is the probability for transition to any of the Rb(^2P) channels; the thin green (light gray) line is that for a transition to any of the ground $^{2,4}\Sigma$ channels; the dots mark the probability of staying in the $^2\Delta$ channel space. The arrow marks the energy at which the $^2P_{3/2}$ channels become open.

functions, due to memory constraints, compared with 42 and 80 for the converged R-matrix calculation. [An R-matrix calculation with this smaller basis produces results that are qualitatively similar to the converged results, in terms of the magnitude of the various partial cross sections as a function
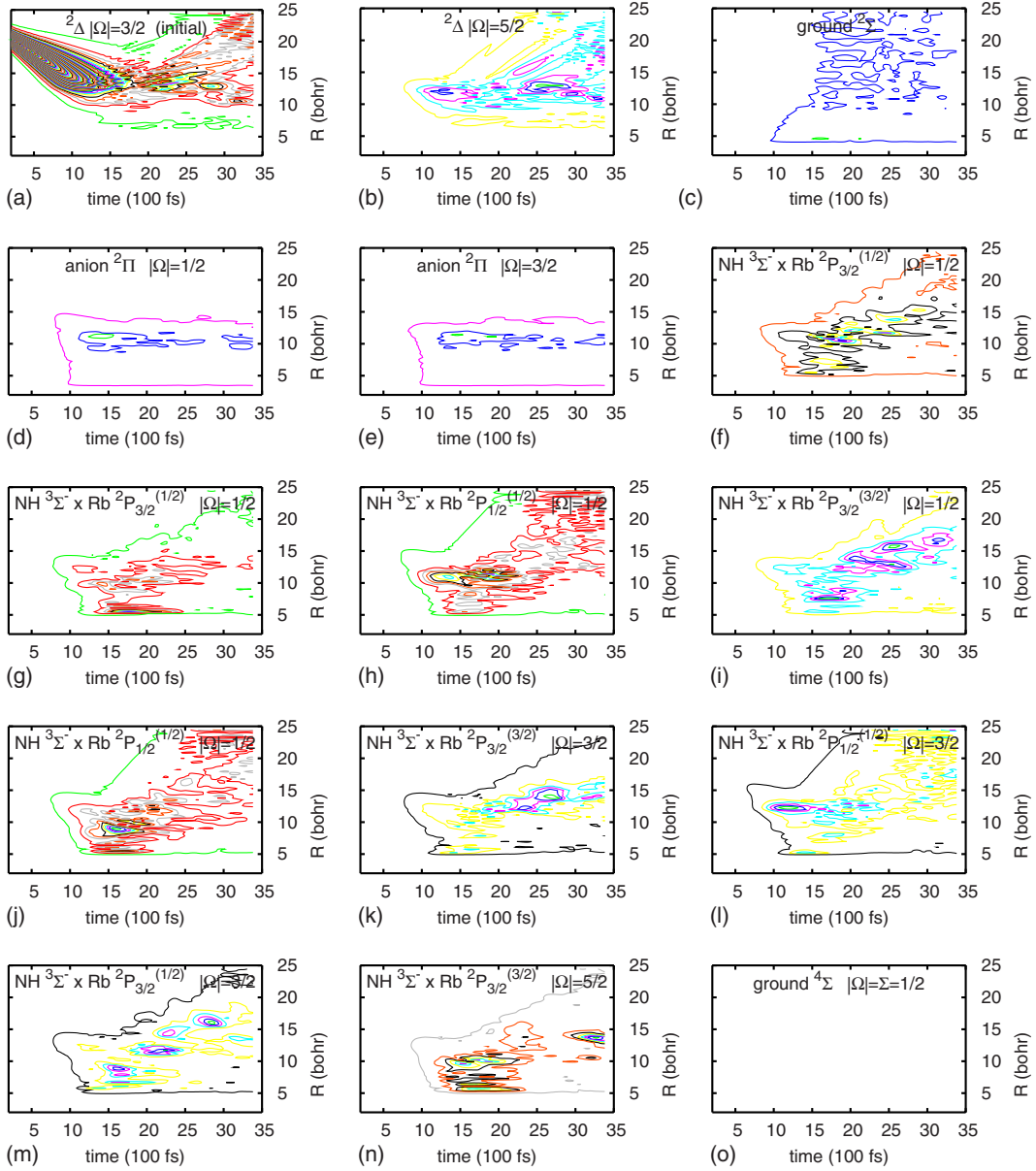
FIG. 6. (Color online) Results of time-dependent wave-packet propagation described in the text. The density, in arbitrary units, integrated over γ, on each electronic channel is shown as a function of the time of propagation and the value of R. The results for the last $^4\Sigma$ state are the same as the one shown, i.e., insufficient density to be visible on the plot. The first contour is at $\frac{1}{10}$th the value of the second one, and the spacing is linear. The states are in the same order (left to right, top to bottom) as in Table I.

of energy, but with peaks significantly altered.] We used 960 Gauss-Lobatto elements with four points per element and an element size of $\frac{2}{90}a_0$, beginning at $3.4a_0$.

We employ a Lanczos propagator of order 12 with variable step size. The step size is determined by requiring that the relative error between the 12th-order and the 11th-order propagator results be less than 2×10^{-7}; we found that this error criterion was sufficient to ensure convergence of observables such as the expectation value and standard deviation of the radial coordinate on every potential-energy surface. The step size ranged from approximately 0.12 to 0.25 fs and was most typically approximately 0.2 fs. After an initial period of propagation in which the wave packet traveled inward of $20a_0$, the scattered wave function was absorbed by

the masking function $f(R)$, where at every time step $\Psi(t) \to f(R)\Psi(t)$ and

$$f(R) = \begin{cases} 1 & (R < 20) \\ \exp\left[-A\Delta t \cot\left(\pi\frac{R-20}{R_0-20}\right)\right] & (R \geq 20), \end{cases} \quad (5)$$

where R_0 is the end of the grid at $24.7\bar{3}a_0$, Δt is the step size, and the constant A is 5×10^{-5} atomic units.

The propagated incident Gaussian wave packet, with a width of $\sqrt{2}$ bohr in the R degree of freedom, starts in the lowest adiabatic (in R) channel of the $^2\Delta$ $|\Omega|=\frac{3}{2}$ electronic state, at a radius of $R=22a_0$. The wave packet is given an initial translational energy of 90 cm^{-1}, such that the lower
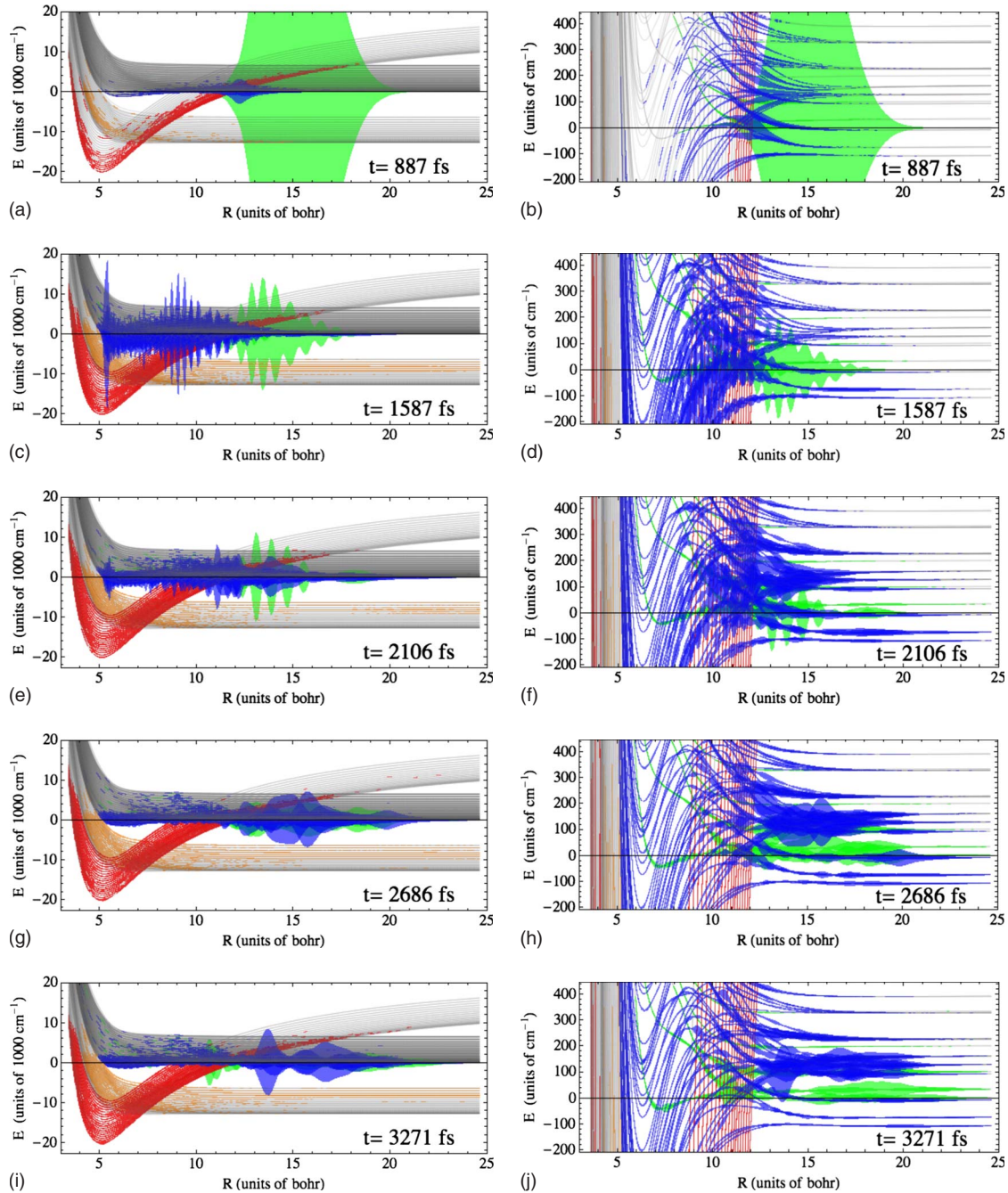
FIG. 7. (Color online) Time-dependent wave-packet propagation described in the text. Each frame is a snapshot of the wave packets on each adiabatic curve. The curves are drawn with black lines and the wave packets on each of these curves are drawn above and below the corresponding curve. Each adiabatic curve corresponds to a different diabatic electronic channel and these are distinguished by the color of the wave packet (online only). Green denotes the $^2\Delta$ channels including the incident one, blue denotes Rb(^2P) channels, red denotes the anion state, and orange denotes the ground-state $^2\Sigma$ and $^4\Sigma$ channels. For readers of the black and white version, the electronic states may be distinguished as follows. The curves in the left panels fall into three groups according to their asymptotes, which from lowest to highest energy are 1) ground state $^2\Sigma$ and $^4\Sigma$; 2) $^2\Delta$ and Rb ^2P; 3) anion. The $^2\Delta$ and Rb ^2P curves may be distinguished in the right panels, where the former appear light gray and the latter appear dark gray. The wave packet is incident in the ground rotational $^2\Delta|\Omega|=3/2$ channel.

Rb $^2P_{1/2}$ channels are open, but the $^2P_{3/2}$ channels are closed, although the bandwidth of the initial wave packet is 18 cm^{-1}.

The results are shown in Figs. 6 and 7. Figure 6 shows the probability density as a function of time and the scattering coordinate R, summed over the adiabatic states (in R) for each diabatic electronic channel. In this figure, the initial state corresponds to the upper left-hand panel. In Fig. 7, the initial state is colored green (online) and corresponds to the large area of probability visible in the upper two panels. Both plots show that the density on the initial state electronic surface does not penetrate much beyond $R=10.0a_0$; instead, it

couples to several of the Rb ^2P surfaces and also reflects. The cut of the surfaces at linear geometry in Fig. 2(b) shows the innermost extent of the attractive part of the initial state $^2\Delta$ surface, near $R = 7.0a_0$, whereas for the opposite Rb-H-N geometry the potential well extends only to approximately $10.0a_0$. It is therefore likely that the reflected part of the initial wave packet, most clearly visible in Fig. 6, comes from configurations near linear Rb-H-N geometry, and that the remaining flux is lost to the other surfaces within $10.0a_0$.

Some immediate coupling evidently occurs among the initial state and all of the Rb (^2P) states, as is clear from the similar shape of the lowest contour line in the corresponding panels of Fig. 6 around 1000 fs. The coupling seems to be strongest between the initial $^2\Delta$ state and the Rb($^2P_{1/2}$) $\times$ NH($^3\Sigma^-\Sigma^{NH}$=0), $|\Omega| = \frac{1}{2}$ state (the eighth state in Table I and Fig. 6). The transition between the initial Rb (^2S) $\times$ NH ($^1\Delta$) and this one is the only transition corresponding to a conservation of the projection of spin angular momentum on NH (Σ^{NH}) along with a transition to the Rb $^2P_{1/2}$ state. This electronic transition does not conserve the projection of the electronic angular momentum on the NH axis and therefore must be driven at nonlinear geometries.

Figure 7 shows the density on each adiabatic (in R) curve, colored (online) according to the electronic channel index. In viewing this figure one should keep in mind that there is electronic coupling between these curves, which represent the energies of adiabatic (in R) basis functions calculated on each diabatic electronic surface. In particular, the coupling among some of the excited state curves and the ground-state sigma curves means that there is repulsion on the excited state curves and attraction on the ground-state curves that is not represented in this figure.

This figure shows that the coupling is indeed strongest, earliest, to one of the Rb ($^2P_{1/2}$) channels, which rises, from large R to small R around $12a_0$, and that correlates to Rb($^2P_{1/2}$)+NH($^3\Sigma^-$$j$=1). Although some red and orange (online) are visible on the left-hand side of this figure, showing the large view including all of the corresponding anion and ground-state sigma curves, the bulk of the density resides clearly on electronic states involved in the quenching reaction.

Despite the fact that the wave-function amplitude on the anion $^2\Pi$ curves never achieves a large value, these states have significant influence upon the dynamics, as would be expected from the large avoided crossings that they create with some of the Rb ^2P surfaces in the electronically adiabatic picture. R-matrix calculations performed without these diabatic states produced electronically inelastic cross sections markedly different (and smaller) than the ones shown in Fig. 5. The coupling to the anion surfaces clearly involves a large amount of rotational excitation of the NH fragment, as can be seen from the fact that all of the adiabatic curves corresponding to this electronic state have amplitude on them [colored red (online) in Fig. 7].

Because the time-dependent calculation shows that the transition is strongest from the initial state to a Rb $^2P_{1/2}$

state, it corroborates our estimate that the avoided crossings around $14.7a_0$ between components of the higher-energy closed Rb $^2P_{3/2}$ surfaces and the $^2\Delta$ states, caused by the long-range dipole-quadrupole interaction, are sufficiently sharp such that they do not provide a good coupling mechanism for the quenching reaction (at least for the energy considered in this time-dependent calculation). Instead, the evidence suggests that the avoided crossings and conical intersections involving the $^2\Delta$ surface and the Rb ^2P surfaces farther in, caused by the fact that the anion surface drops down steeply and undergoes broad avoided crossings with these surfaces, drive the wave packet onto the Rb $^2P_{1/2}$ surfaces. A more thorough analysis is deferred to a forthcoming publication.

The time-dependent treatment corroborates the result of the R-matrix calculations that the coupling to the ground NH($^3\Sigma^-$)$\times$Rb(^2S) electronic state is relatively small, whereby most of the outgoing flux avoids these channels. The quartet components of this state seem uninvolved in the quenching reaction for the energy studied, as is clear from Fig. 6. A modest flux is seen in the doublet ground-state sigma component, much less than in the Rb ^2P channels, in agreement with the results of the R-matrix calculations. Thus, it appears that the quenching reaction is both efficient and selective.

V. CONCLUSION

These preliminary results show that the quenching reaction Rb(^2S)+NH($^1\Delta$)$\rightarrow$Rb($^2P_{1/2}$)+NH(X $^3\Sigma^-$) does indeed proceed with a high probability as may have been expected due to the near degeneracy of the electronic states involved. The reaction is selective, yielding markedly less ground electronic state products. The coupling mechanism is seen to involve the complicated set of avoided crossings and conical intersections that occur inward of $14.7a_0$, not those due to the long-range interactions. A more complete study will be published in the future, thoroughly analyzing the dynamics that occurs between the many electronic states involved in the system, analyzing the effect of the mixing of electronic and spin angular momenta with rotational angular momentum (the Renner-Teller and the spin Renner-Teller effects), and providing reaction rates for comparison with experiment.

[1] W. Hack, in *N-Centered Radicals*, edited by Z. B. Alfassi (Wiley, Chirchester, 1998), pp. 413–466.

[2] A. P. C. Mann and D. A. Williams, Mon. Not. R. Astron. Soc. **209**, 33 (1984).

[3] I. W. M. Smith, Angew. Chem. **45**, 2842 (2006).

[4] W. R. Anderson, L. J. Decker, and A. J. Kotlar, Combust. Flame **48**, 179 (1982).

[5] J. L. Rinnenthal and K. H. Gericke, J. Mol. Spectrosc. **198**, 115 (1999).

[6] T. G. Slanger and R. A. Copeland, Chem. Rev. (Washington, D.C.) **103**, 4731 (2003).

[7] N. Balakrishnan and A. Dalgarno, Chem. Phys. Lett. **341**, 652 (2001).

[8] K. Burnett, P. S. Julienne, P. D. Lett, E. Tiesinga, and C. J. Williams, Nature (London) **416**, 225 (2002).

[9] P. Zoller, Nature (London) **417**, 493 (2002).

[10] M. W. Zwierlein, C. A. Stan, C. H. Schunck, S. M. F. Raupach, S. Gupta, Z. Hadzibabic, and W. Ketterle, Phys. Rev. Lett. **91**, 250401 (2003).

[11] J. R. Bochinski, E. R. Hudson, H. J. Lewandowski, and J. Ye, Phys. Rev. A **70**, 043410 (2004).

[12] R. V. Krems, Int. Rev. Phys. Chem. **24**, 99 (2005).

[13] M. Qiu *et al.*, Science **311**, 1440 (2006).

[14] M. H. Anderson, J. R. Ensher, M. R. Matthews, C. E. Weiman, and E. A. Cornell, Science **269**, 198 (1995).

[15] C. J. Myatt, E. A. Burt, R. W. Ghrist, E. A. Cornell, and C. E. Wieman, Phys. Rev. Lett. **78**, 586 (1997).

[16] J. D. Weinstein, R. deCarvalho, T. Guillet, B. Friedrich, and J. M. Doyle, Nature (London) **395**, 921 (1998).

[17] L. Santos, G. V. Shlyapnikov, P. Zoller, and M. Lewenstein, Phys. Rev. Lett. **85**, 1791 (2000).

[18] D. Wang, J. Qi, M. F. Stone, O. Nikolayeva, H. Wang, B. Hattaway, S. D. Gensemer, P. L. Gould, E. E. Eyler, and W. C. Stwalley, Phys. Rev. Lett. **93**, 243005 (2004).

[19] J. M. Sage, S. Sainis, T. Bergeman, and D. DeMille, Phys. Rev. Lett. **94**, 203001 (2005).

[20] B. C. Sawyer, B. L. Lev, E. R. Hudson, B. K. Stuhl, M. Lara, J. L. Bohn, and J. Ye, Phys. Rev. Lett. **98**, 253002 (2007).

[21] S. Y. T. van de Meerakker, R. T. Jongma, H. L. Bethlem, and G. Meijer, Phys. Rev. A **64**, 041401(R) (2001).

[22] D. Egorov, W. C. Campbell, B. Friedrich, S. E. Maxwell, E. Tsikata, L. D. van Buuren, and J. M. Doyle, Eur. Phys. J. D **31**, 307 (2004).

[23] W. C. Campbell, E. Tsikata, Hsin-I Lu, L. D. van Buuren, and J. M. Doyle, Phys. Rev. Lett. **98**, 213001 (2007).

[24] S. Hoekstra, M. Metsala, P. C. Zieger, L. Scharfenberg, J. J. Gilijamse, G. Meijer, and S. Y. T. van de Meerakker, Phys. Rev. A **76**, 063408 (2007).

[25] M. T. Hummon, W. C. Campbell, Hsin-I Lu, E. Tsikata, Y. Wang, and J. M. Doyle, Phys. Rev. A **78**, 050702(R) (2008).

[26] P. Soldan, P. Zuchowski, and J. Hutson, e-print arXiv:0901.2493.

[27] P. Soldan and J. M. Hutson, Phys. Rev. Lett. **92**, 163202 (2004).

[28] M. Tacconi, L. Gonzalez-Sanchez, E. Bodo, and F. A. Gianturco, Phys. Rev. A **76**, 032702 (2007).

[29] M. Tacconi, E. Bodo, and F. A. Gianturco, Theor. Chem. Acc. **117**, 649 (2007).

[30] M. Lara, J. L. Bohn, D. Potter, P. Soldan, and J. M. Hutson, Phys. Rev. Lett. **97**, 183201 (2006).

[31] M. Lara, J. L. Bohn, D. E. Potter, P. Soldan, and J. M. Hutson, Phys. Rev. A **75**, 012704 (2007).

[32] R. V. Krems, H. R. Sadeghpour, A. Dalgarno, D. Zgid, J. Klos, and G. Chalasinski, Phys. Rev. A **68**, 051401(R) (2003).

[33] H. Cybulski, R. V. Krems, H. R. Sadeghpour, A. Dalgarno, J. Kross, G. C. Groenenboom, A. van der Avoird, D. Zgid, and G. Chatasinski, J. Chem. Phys. **122**, 094307 (2005).

[34] M. L. Gonzalez-Martinez and J. M. Hutson, Phys. Rev. A **75**, 022702 (2007).

[35] P. S. Zuchowski and J. M. Hutson, Phys. Rev. A **78**, 022701 (2008).

[36] P. Zuchowski and J. Hutson, Phys. Rev. A **79**, 062708 (2009).

[37] G. S. F. Dhont, J. H. van Lenthe, G. C. Groenenboom, and A. van der Avoird, J. Chem. Phys. **123**, 184302 (2005).

[38] J. E. Sansonetti, J. Phys. Chem. Ref. Data **35**, 301 (2006).

[39] H. L. Bethlem, G. Berden, and G. Meijer, Phys. Rev. Lett. **83**, 1558 (1999).

[40] S. Y. T. van de Meerakker, P. H. M. Smeets, N. Vanhaecke, R. T. Jongma, and G. Meijer, Phys. Rev. Lett. **94**, 023004 (2005).

[41] H. Lishka, R. Shepard, F. B. Brown, and I. Shavitt, Int. J. Quantum Chem., Quantum Chem. Symp. **20**, 91 (1981).

[42] R. Shepard, I. Shavitt, R. M. Pitzer, D. C. Comeau, M. Pepper, H. Lishka, P. G. Szalay, R. Ahlrichs, F. B. Brown, and J. Zhao, Int. J. Quantum Chem., Quantum Chem. Symp. **34**, 149 (1988).

[43] H. Lishka *et al.*, COLUMBUS: An *Ab Initio* Electronic Structure Program, Release 5.9.1, 2006.

[44] L. von Szentpaly, P. Fuentealba, H. Preuss, and H. Stoll, Chem. Phys. Lett. **93**, 555 (1982).

[45] P. Fuentealba, H. Stoll, L. v. Szentpaly, P. Schwerdtfeger, and H. Preuss, J. Phys. B **16**, L323 (1983).

[46] W. Domcke and G. Stock, Adv. Chem. Phys. **100**, 1 (1997).

[47] J. T. H. Dunning, J. Chem. Phys. **90**, 1007 (1989).

[48] A. Macias and A. Riera, J. Phys. B **11**, L489 (1978).

[49] H.-J. Werner and W. Meyer, J. Chem. Phys. **74**, 5802 (1981).

[50] C. Petrongolo, J. Chem. Phys. **89**, 1297 (1988).

[51] S. Sukiasyan and H.-D. Meyer, J. Phys. Chem. A **105**, 2604 (2001).

[52] K. P. Huber and G. Herzberg, *Molecular Spectra and Molecular Structure IV: Constants of Diatomic Molecules* (Van Nostrand Reinhold Co., New York, 1979).

[53] K. L. Baluja, P. G. Burke, and L. A. Morgan, Comput. Phys. Commun. **27**, 299 (1982).

[54] A. S. Dickinson and P. R. Certain, J. Chem. Phys. **49**, 4209 (1968).

[55] J. C. Light, I. P. Hamilton, and J. V. Lill, J. Chem. Phys. **82**, 1400 (1985).

[56] G. C. Corey and D. Lemoine, J. Chem. Phys. **97**, 4115 (1992).

[57] T. N. Rescigno and C. W. McCurdy, Phys. Rev. A **62**, 032706 (2000).

[58] O. I. Tolstikhin, S. Watanabe, and M. Matsuzawa, J. Phys. B **29**, L389 (1996).